Thermoelastic enhancement of the magnonic spin Seebeck effect in thin films and bulk samples

L. Chotorlishvili,[1] X.-G. Wang,[2] Z. Toklikishvili,[3] and J. Berakdar[1]
[1]*Institut für Physik, Martin-Luther Universität Halle-Wittenberg, D-06120 Halle/Saale, Germany*
[2]*School of Physics and Electronics, Central South University, Changsha 410083, China*
[3]*Faculty of Mathematics and Natural Sciences, Tbilisi State University, Chavchavadze avenue 3, 0128 Tbilisi, Georgia*

(Received 6 December 2017; revised manuscript received 9 February 2018; published 16 April 2018)

A nonuniform temperature profile may generate a pure spin current in magnetic films, as observed, for instance, in the spin Seebeck effect. In addition, thermally induced elastic deformations may set in that could affect the spin current. A self-consistent theory of the magnonic spin Seebeck effect including thermally activated magnetoelastic effects is presented, and analytical expressions for the thermally activated deformation tensor and dispersion relations for coupled magnetoelastic modes are obtained. We derive analytical results for bulk (three-dimensional) systems and thin magnetic (two-dimensional) films. We observe that the displacement vector and the deformation tensor in bulk systems decay asymptotically as $u \sim 1/R^2$ and $\varepsilon \sim 1/R^3$, respectively, while the decays in thin magnetic films proceed slower, following $u \sim 1/R$ and $\varepsilon \sim 1/R^2$. The dispersion relations evidence a strong anisotropy in the magnetic excitations. We observe that a thermoelastic steady-state deformation may lead to both an enchantment and a reduction of the gap in the magnonic spectrum. The reduction of the gap increases the number of magnons contributing to the spin Seebeck effect and offers new possibilities for the thermoelastic control of the spin Seebeck effect.

DOI: 10.1103/PhysRevB.97.144409

I. INTRODUCTION

By virtue of magnetoelastic coupling elastic deformations may trigger a magnetization dynamics, and (magneto)elastic waves maybe launched due to spin motion. The study of elastically activated magnetic dynamics in ferro- and antiferromagnetic materials dates back to the late 1950s, starting with seminal independent works by Akhlezer *et al.* [1] and Kittel [2]. Further findings came from the discovery of the magnetoelastic gap [3–5] that bears some resemblance to spontaneous symmetry breaking [6]. Since the magnetically excited elastic waves affect in turn the magnetization dynamics, the established magnetoelastic gap, being a second-order effect, is proportional to the square of the magnetoelastic coupling constant. Thus, the magnetoelastic gap is usually quite small compared to the gap in the magnonic spectrum which is induced, for instance, by a magnetocrystalline anisotropy or by external field terms.

A thermal heating leading to a steady-state elastic deformation may serve as an alternative for activating (magneto)elastic modes that occur in ferromagnetic films and heterostructures [7–17]. Elasticity involving nonisothermal deformations is part of the well-established field of thermoelasticity [18,19]. An important question in the context of the present paper is to what extent a steady-state thermoelastic deformation influences the magnetoacoustic effect. Due to the grossly different timescales of the dynamics, a steady-state thermoelastic deformation is swiftly established (meaning equilibrated with the external thermal bath) and is basically unaffected by the much slower magnetization dynamics. The magnetization dynamics may well be sensitive to thermoelastic deformation, however. We will investigate here the theoretical aspects of thermal magnetoacoustics, i.e., thermally activated magnetoelastic effects with a special focus on phenomena of interest to the active field of spin caloritronics [20–36]. Experimentally, the utilization of elasticity to steer the magnetic dynamics is meanwhile accessible in a variety of settings. For instance, Rayleigh surface acoustic waves that may couple to spin ordering can be generated by irradiation with laser pulses [37]. This process may well be accompanied by local heating spreading away from the laser spot, which in turn may launch temporally a spin Seebeck current. Heating by laser pulses was employed for experiments concerning the time-resolved spin Seebeck effect [38]. Simulations of the time-resolved spin Seebeck effect were presented in Ref. [39].

A comprehensive study of the thermal magnetoacoustic effect should encompass both heating and elasticity aspects. Heating, for instance, by laser pulses leads to a buildup of a nonuniform temperature distribution and possibly a temporal magnonic spin Seebeck effect. Nonisothermal deformations may also contribute to magnetoelastic activation of magnonic spin current. For example, considering that nonisothermal deformation of the thin film may reduce the gap in the magnonic spectrum, the spin Seebeck effect may well be modified, for a reduction in the magnonic gap increases the number of magnons contributing to the spin Seebeck effect. In what follows we explore the link between the nonisothermal deformation $(\mathbf{R})$ tensor $\boldsymbol{\varepsilon}_{\xi\zeta}(\mathbf{R})$ and the magnonic energy spectrum $\omega^2(q,\mathbf{R},\boldsymbol{\varepsilon}_{\xi\zeta}(\mathbf{R}))$ at the wave vector q. We derive analytical solutions for the deformation tensor and implement them for the thermally activated magnetoelastic dynamics. We analyze in detail the three-dimensional (3D) case of a bulk sample and compare it with a two-dimensional (2D) case of a thin film. Analytical results are complemented by full numerical micromagnetic simulations.

This paper is organized as follows: in Sec. II we introduce the model, and in Sec. III we discuss the generalities of the magnetothermal effect and derive explicit analytical expressions

for the displacement vector and for the deformation tensor for local and nonlocal heat sources. Section IV is dedicated to the dispersion relations for thermally excited magnetoelastic magnonic modes. In Sec. V we present analytical results for the spin-wave dispersion in thin films, and in Sec. VI we analyze the results of the micromagnetic numerical calculations, followed by a summary and conclusions.

II. GENERAL FORMULATION

We study the transversal magnetic dynamics of a magnetoelastically coupled system as described by the deformation-dependent time evolution of the unit vector field $\mathbf{M}$. We will work along a Landau-Ginzburg approach starting from the energy functional

$$H = H_m + U_{\rm mel}(\mathbf{R}). \tag{1}$$

The magnetic part H_m can be broken down essentially into the exchange, magnetocrystalline anisotropy, and Zeeman terms (summation over repeated indexes is assumed),

$$H_m = A_{\xi\zeta}\frac{\partial \mathbf{M}}{\partial x_\xi}\frac{\partial \mathbf{M}}{\partial x_\zeta} + K_{\xi\zeta}\mathbf{M}_\xi\mathbf{M}_\zeta - \mathbf{B}\cdot\mathbf{M}, \tag{2}$$

where $A_{\xi\zeta}$ is the exchange stiffness, $K_{\xi\zeta}$ quantifies the magnetocrystalline anisotropy energy contribution, and $\mathbf{B}$ is an external magnetic field. The magnetoacoustic energy density $U_{\rm mel}(\mathbf{R})$ reads

$$U_{\rm mel}(\mathbf{R}) = \frac{B_1}{M_s^2}M_\xi^2\varepsilon_{\xi\xi} + \frac{B_2}{M_s^2}M_\xi M_\zeta \varepsilon_{\xi\zeta}. \tag{3}$$

Here M_S is the saturation magnetization; $M_\xi(\mathbf{R}), M_\zeta(\mathbf{R})$ are the magnetization components along the $\xi,\zeta = x,y,z$ axes; and B_1, B_2 are the magnetoelastic constants. The deformation tensor has the explicit form

$$\varepsilon_{\xi\zeta}(\mathbf{R}) = \frac{1}{2}\left(\frac{\partial u_\xi(\mathbf{R})}{\partial x_\zeta} + \frac{\partial u_\zeta(\mathbf{R})}{\partial x_\xi}\right), \tag{4}$$

where $u_\xi(\mathbf{R})$ is the component of the displacement vector. The stress tensor of the system $\sigma_{\xi\zeta}$ satisfies the relation $F_\xi = \frac{\partial \sigma_{\xi\zeta}}{\partial x_\zeta}$, where F_ξ is the component of the external force which is applied to the system. In the absence of an external force, equilibrium requires that $\frac{\partial \sigma_{\xi\zeta}}{\partial x_\zeta} = 0$. The stress and the deformation tensors are interrelated via the algebraic relation

$$\sigma_{\xi\zeta} = \frac{E}{1+\sigma}\left(\varepsilon_{\xi\zeta} + \frac{\sigma}{1-2\sigma}\varepsilon_{\xi\xi}\delta_{\xi\zeta}\right). \tag{5}$$

Here E is the elasticity modulus, and σ is Poisson's constant.

III. MAGNETOTHERMAL EFFECTS IN THE 3D BULK SYSTEM

We will be dealing with small-amplitude displacements in the 3D bulk system. Proceeding in a standard way, the equation of motion for elastic waves without an applied thermal bias is [19]

$$\rho\frac{d^2\mathbf{u}}{dt^2} = \frac{E}{2(1+\sigma)}\triangle\mathbf{u} + \frac{E}{2(1+\sigma)(1-2\sigma)}\nabla(\nabla\cdot\mathbf{u}). \tag{6}$$

In the presence of an applied thermal bias ∇T, one derives the equation of motion for the thermoelastic waves by adding the temperature term,

$$\rho\frac{d^2\mathbf{u}}{dt^2} = \frac{E}{2(1+\sigma)}\triangle\mathbf{u} + \frac{E}{2(1+\sigma)(1-2\sigma)}\nabla(\nabla\cdot\mathbf{u}) - \frac{E\kappa\nabla T}{3(1-2\sigma)}. \tag{7}$$

Here κ is the thermal expansion coefficient, and ∇T is a temperature gradient which is due to laser heating, for instance. Equation (7) describes the dynamics of the elastic modes coupled to the magnetization dynamics via magnetoelastic coupling $U_{\rm mel}(\mathbf{R})$ [see Eq. (3)]. Classically, the magnetization dynamics follows the stochastic Landau-Lifshitz-Gilbert equation

$$\frac{\partial \mathbf{M}(\mathbf{R},t)}{\partial t} = -\gamma\mathbf{M}(\mathbf{R},t)\times(\mathbf{H}_{\rm eff}+\mathbf{h}) - \frac{A}{\hbar M_S}\mathbf{M}(\mathbf{R},t)\times\nabla^2\mathbf{M}(\mathbf{R},t) + \frac{\alpha}{M_s}\mathbf{M}(\mathbf{R},t)\times\frac{\partial \mathbf{M}(\mathbf{R},t)}{\partial t}, \tag{8}$$

with the deterministic effective field $\mathbf{H}^{\rm eff} = -\frac{\delta \mathbf{H}}{\delta \mathbf{M}}$ and $H = H_m + U_{\rm mel}(\mathbf{R})$ complemented by a random field $h(\mathbf{R},t)$ due to a Gaussian white noise with the autocorrelation function

$$\langle h_i(t,\mathbf{R})h_j(t',\mathbf{R}')\rangle = \frac{2k_BT(\mathbf{R})\alpha}{\gamma M_S a^3}\delta_{ij}\delta(\mathbf{R}-\mathbf{R}')\delta(t-t'). \tag{9}$$

Here α is the Gilbert damping, $\gamma = 1.76\times10^{11}$ (T s)$^{-1}$ is the gyromagnetic ratio, $T(\mathbf{R})$ is the local temperature formed in the system, and M_S is the saturation magnetization. The magnonic spin current tensor is evaluated as

$$J_j^{\mathbf{M}_\xi} = \frac{A}{\hbar M_S}\varepsilon_{\xi\mu\nu}\mathbf{M}_\mu\nabla_j\mathbf{M}_\nu. \tag{10}$$

Latin indices refer to the spatial components, while Greek indices refer to the spin projections. Since the magnetoelectric term is part of the effective field in Eq. (8), it is expected to contribute to the spin current (10). The temporal, spatially nonuniform temperature profile $\nabla T(\mathbf{R},t)$ can be inferred from the solution of the heat equation with the appropriate source term $I(\mathbf{R},t)$. Explicitly, this equation reads [39]

$$\frac{\partial T(\mathbf{R},t)}{\partial t} = \frac{k_{ph}}{\rho C}\nabla^2T(\mathbf{R},t) + I(\mathbf{R},t). \tag{11}$$

C is the phonon heat capacity, k_{ph} is the phononic thermal conductivity, and ρ is the mass density. The imparted energy, e.g., by laser pulses is usually not completely absorbed by the system but is partially dissipated. Thermal losses can be incorporated in a realistic modeling of the laser heating process. For more details we refer readers to Ref. [39]. It is important to consider the relevant timescales. When the characteristic timescale of the heating process is faster than the magnetization dynamics (i.e., the phonon relaxation timescale and the time interval between laser pulses are shorter than the precession time $\tau < 1/\gamma H_{\rm eff}$), the magnetic system experiences an effective temperature which is deduced from an

average over the much faster timescales. In this case, instead of the coupled set of equations (7), (8), and (11), we can explore a steady-state problem. After some algebra, we derive for this case the solution of the elasticity equation for the displacement vector valid for an arbitrary averaged, nonuniform effective temperature as

$$\mathbf{u}(\mathbf{R}) = -\frac{\kappa(1+\sigma)}{12\pi(1-\sigma)}\nabla_{\mathbf{R}}\int\frac{T(\mathbf{R_1})-T_0}{|\mathbf{R}-\mathbf{R_1}|}d^3\mathbf{R_1}. \quad (12)$$

The spatial temperature profile $T(\mathbf{R})$ is arbitrary, satisfying the asymptotic boundary condition $T_0 = T(|\mathbf{R}-\mathbf{R}_0| \to \infty)$, where $\mathbf{R}_0$ defines the region where the heat source is localized. In what follows we consider two different temperature profiles formed in the system due to the laser heating.

A. Pointlike heat sources

Let us assume that the energy pumped, for instance, via laser irradiation is localized such that $T(\mathbf{R}_1) - T_0 = \frac{Q}{C}\delta(\mathbf{R}_1)$, where Q is the heat released by the laser and C is the heat capacity of the material. The displacement vector $\mathbf{u}(\mathbf{R})$ reads for this case

$$\mathbf{u}(\mathbf{R}) = \frac{\kappa(1+\sigma)Q}{12\pi(1-\sigma)C}\frac{\mathbf{R}}{R^3}. \quad (13)$$

With Eq. (13) we obtain the explicit form of the deformation tensor

$$\boldsymbol{\varepsilon}_{\xi\zeta}(\mathbf{R}) = \frac{\kappa(1+\sigma)}{12\pi(1-\sigma)}\frac{Q}{C}\frac{1}{R^3}\left\{\delta_{\xi\zeta} - \frac{x_\xi x_\zeta}{R^2}\right\}. \quad (14)$$

Point heat sources are an idealization. In reality for thin films the temperature profile decays exponentially, as proved by the exact numerical solution of Eq. (11). Therefore, we explore an exponential temperature profile.

B. Extended heat sources

Let us consider an exponential temperature profile matching the numerical solutions of the heat equation with a nonlocal, i.e., extended, heating source I. $T(\mathbf{R}_1) = \frac{Q_1}{C}\exp(-\beta|\mathbf{R}_1|) + T_0$, where β is the characteristic decay length and Q_1 is the density of the heat released by the laser in the vicinity of the point $\mathbf{R}_1 = 0$. The temperature in the heating point $T(0) = Q_1/C + T_0$, and the asymptotic $T(|\mathbf{R}_1| \to \infty) = T_0$. Following some involved calculations for the displacement vector, we infer

$$\mathbf{u}(\mathbf{R}) = -\frac{\kappa(1+\sigma)Q_1}{3(1-\sigma)C}\nabla_{\mathbf{R}} \times\left\{\frac{2}{\beta^3 R} - e^{-\beta R}\left(\frac{2}{\beta^3 R} + \frac{1}{\beta^2}\right)\right\}. \quad (15)$$

With this relation we obtain an explicit form of the deformation tensor as

$$\boldsymbol{\varepsilon}_{\xi\zeta}(\mathbf{R}) = -\frac{\kappa(1+\sigma)Q_1}{3(1-\sigma)C} \times\left\{\delta_{\xi\zeta}F_1(\beta R) + \frac{x_\xi x_\zeta}{R^2}F_2(\beta R)\right\}. \quad (16)$$

For brevity we introduced the notations

$$F_1(y) = \{\exp(-y)(1+2/y) - 2/y^2[1-\exp(-y)]\}/y$$

and

$$F_2(y) = [6 - 6\exp(-y) - y\exp(-y)(6+3y+y^2)]/y^3.$$

Formally, Eqs. (13)–(16) exhibit a nonphysical divergence in the limit $\mathbf{R} \to 0$. We note however, in a coarse-grained approach the unit cell is nondeformable. Therefore, the minimal $\mathbf{R} \to 0$ for which the study of the deformation makes sense is larger than the size of the coarse-grained cell $|\mathbf{R} \to 0| > a$, and $a \approx 10$ nm.

While in the general case the expression for the displacement vector (15) is quite involved, it is easy to see that in the asymptotic limit of the large $R \mapsto \infty$ we have a decay $1/R^2$.

C. Linear temperature profile

A linear temperature profile has played a central role in the spin Seebeck experiments [40–42]. Thus, we consider a temperature profile of the following form: $T(R) = -(T'-T_0)R/R_{\max} + T'$, where $T' > T_0$ and the temperature at the edges is equal to $T(0) = T'$, $T(R_{\max}) = T_0$. Implementing this linear temperature profile, we infer for the displacement vector

$$\mathbf{u}(\mathbf{R}) = \frac{\kappa(1+\sigma)(T'-T_0)\mathbf{R}}{9(1-\sigma)}\left(1 - \frac{3R}{4R_{\max}}\right), \quad (17)$$

and for the deformation tensor we have

$$\varepsilon_{\xi\zeta} = \frac{\kappa(1+\sigma)(T'-T_0)}{9(1-\sigma)} \times\left[\delta_{\xi\zeta}(1-3R/4R_{\max}) - \frac{3x_\xi x_\zeta}{4R_{\max}R}\right]. \quad (18)$$

As we see in the case of a linear temperature gradient, the asymptotic behaviors of the displacement vector and the deformation tensor are different and are nonmonotonic in $R = \sqrt{x^2+y^2+z^2}$. The maximum of the absolute value of the displacement vector corresponds to the case $|\mathbf{u}(\mathbf{R})| = 2R_{\max}/3$.

IV. DISPERSION RELATIONS FOR THERMAL MAGNETOELASTIC SPIN WAVES IN BULK SYSTEMS

Taking into account Eqs. (8) and (13)–(16) and assuming that the ground-state magnetization is aligned parallel to the z axis, we derive the following dispersion relation for the coupled magnetoelastic magnonic modes in the 3D bulk system:

$$\omega^2(q,\mathbf{R}) = \left[\frac{2\gamma A_{\rm ex}}{M_s^2}q^2 + K + \gamma H_0 - \frac{2\gamma B_{12}}{M_s^2}(\varepsilon_{zz}-\varepsilon_{xx})\right] \times\left[\frac{2\gamma A_{\rm ex}}{M_s^2}q^2 + K + \gamma H_0 - \frac{2\gamma B_{12}}{M_s^2}(\varepsilon_{zz}-\varepsilon_{yy})\right] - \left(\frac{2\gamma B_{12}}{M_s^2}\varepsilon_{xy}\right)^2. \quad (19)$$

Here $B_1 = B_2 = B_{12}$ are the magnetoelastic coupling constants.

Obviously, in the absence of the magnetoelastic effect $\boldsymbol{\varepsilon}_{\xi\zeta}(\mathbf{R}) = 0$, the obtained result falls back to the well-known

magnonic dispersion relation. Depending on the values of the components of deformation tensor $\boldsymbol{\varepsilon}_{\xi\zeta}(\mathbf{R})$, the magnetoelastic contribution in the magnonic dispersion relations can be positive or negative. A negative contribution $-\frac{2\gamma B_{12}}{\mu_0 M_s}(\varepsilon_{zz}-\varepsilon_{xx})<0$ or $-\frac{2\gamma B_{12}}{\mu_0 M_s}(\varepsilon_{zz}-\varepsilon_{yy})<0$ decreases the magnonic gap, while a positive contribution leads to an enhancement. Thus, the thermal magnetoelastic effect can be used as a tool to reduce the magnonic gap imposed by the magnetocrystalline anisotropy or by an external magnetic field. A reduction in the gap naturally increases the spin Seebeck effect since it enhances the number of magnons contributing to the spin current. We note that $\boldsymbol{\varepsilon}_{\xi\zeta}(\mathbf{R})$ is a local quantity and can be different for different $\mathbf{R}$. In some particular cases the magnonic gap can be enhanced, and this naturally decreases the spin Seebeck current. After inserting the explicit expression for the deformation tensor $\boldsymbol{\varepsilon}_{\xi\zeta}(\mathbf{R})$ in Eq. (19), we deduce

$$\omega(q,\mathbf{R})=\frac{1}{\hbar}\sqrt{\left(Aq^2+f_R^{(1)}\right)\left(Aq^2+f_R^{(2)}\right)-f_R^{(3)}}. \quad (20)$$

The particular values of the introduced functions $f_R^{(1,2,3)}$ are different for the exponential heat source, for the pointlike heat source, and for the linear temperature profile.

(a) In case of a pointlike heat source we find

$$f_R^{(1)}=\gamma\hbar\left\{\frac{\kappa(1+\sigma)}{6\pi M_s^2(1-\sigma)}\frac{1}{R^2}\frac{Q}{C}B_1(z^2-x^2)+H_0\right\}, \quad (21)$$

$$f_R^{(2)}=\gamma\hbar\left\{\frac{\kappa(1+\sigma)}{6\pi M_s^2(1-\sigma)}\frac{1}{R^2}\frac{Q}{C}B_1(z^2-y^2)+H_0\right\}, \quad (22)$$

$$f_R^{(3)}=\left\{\gamma\hbar\frac{\kappa(1+\sigma)}{6\pi M_s^2(1-\sigma)}\frac{1}{R^2}\frac{Q}{C}B_2xy\right\}^2. \quad (23)$$

(b) In the case of an exponential temperature profile we find

$$f_R^{(1)}=\gamma\hbar\left\{\frac{2\kappa(1+\sigma)Q_1(z^2-x^2)}{3M_s^2R^2(1-\sigma)C}B_1F_2(\beta R)+H_0\right\}, \quad (24)$$

$$f_R^{(2)}=\gamma\hbar\left\{\frac{2\kappa(1+\sigma)Q_1(z^2-y^2)}{3M_s^2R^2(1-\sigma)C}B_1F_2(\beta R)+H_0\right\}, \quad (25)$$

$$f_R^{(3)}=\left\{\gamma\hbar\frac{2\kappa(1+\sigma)Q_1xy}{3M_s^2R^2(1-\sigma)C}B_2F_2(\beta R)\right\}^2. \quad (26)$$

(c) In the case linear temperature profile we deduce

$$f_R^{(1)}=\hbar\gamma\left\{\frac{B_1}{6R_{\max}RM_s^2}\frac{\kappa(1+\sigma)(T_0-T')}{(1-\sigma)}(x^2-z^2)+H_0\right\}, \quad (27)$$

$$f_R^{(2)}=\hbar\gamma\left\{\frac{B_1}{6R_{\max}RM_s^2}\frac{\kappa(1+\sigma)(T_0-T')}{(1-\sigma)}(y^2-z^2)+H_0\right\}, \quad (28)$$

$$f_R^{(3)}=\left\{\hbar\gamma\frac{B_2}{6R_{\max}RM_s^2}\frac{\kappa(1+\sigma)(T_0-T')}{(1-\sigma)}xy\right\}^2. \quad (29)$$

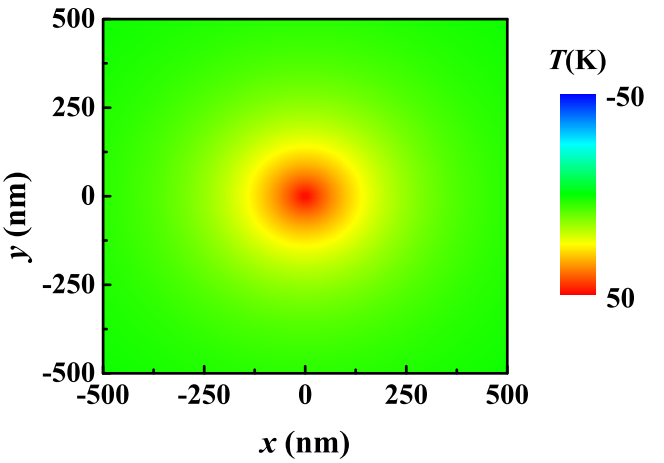

FIG. 1. The temperature profile in the 3D bulk system $T(\mathbf{R_1})=\frac{Q_1}{C}\exp(-\beta|\mathbf{R_1}|)$, formed due to the effect of the extended heat source. The density of the heat released by the laser in the vicinity of the point $R_1=0$ is equal to $Q_1/C=50$ K, and the heat capacity of the nickel $C=502$ J/(kg K). For convenience we present the projection of the temperature profile on the XOY plane by setting $z=0$.

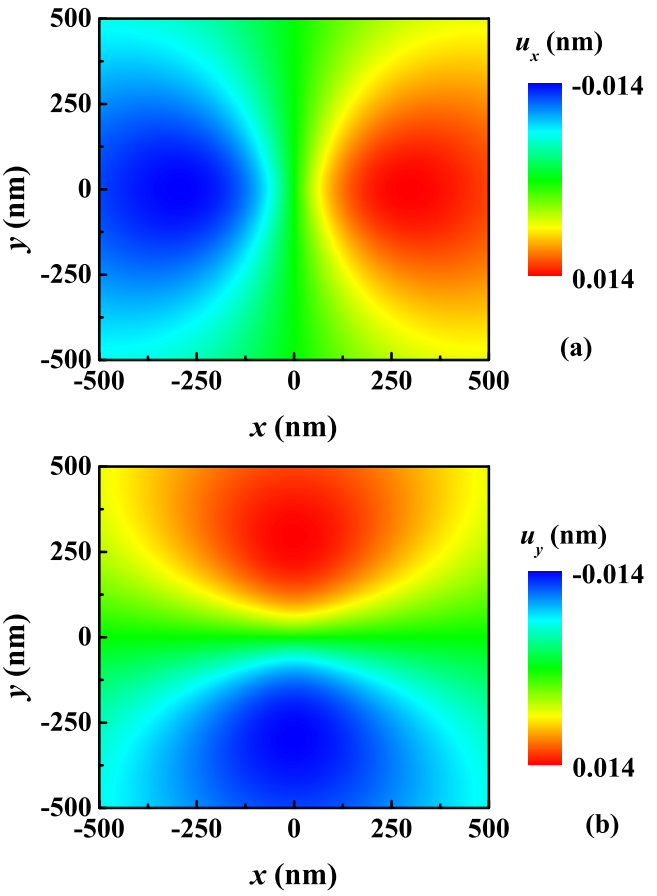

FIG. 2. Displacement tensors (a) u_x and (b) u_y in the 3D bulk system, induced by the exponential temperature profile. The symmetry properties of the displacement tensors u_x and u_y are shown. In particular, the u_x component manifests a mirror symmetry with respect to the reflection $y\to -y$ and antisymmetry with respect to the reflection $x\to -x$. Concerning the component u_y, the behavior is opposite: we find symmetry with respect to the reflection $x\to -x$ and antisymmetry with respect to the reflection $y\to -y$.

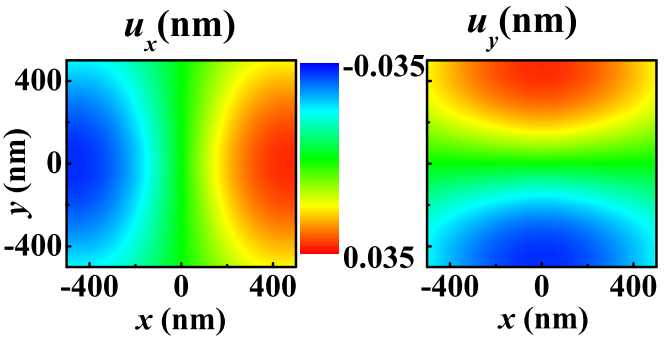

FIG. 3. The displacement vectors in the 3D bulk system u_x and u_y, induced by a linear temperature profile. The temperature in the center is equal to $T(0) = 50$ K, and that at the edges is $T(R_{\max}) = 0$.

As we see from Eqs. (20)–(29), the dispersion relation for mixed magnon-phonon modes are rather complex. The dependence on the spatial variable $\mathbf{R}$ is nonuniform, with an anisotropic character of the magnonic modes. Note that obtained analytical results correspond to the 3D model, while for the sake of simplicity in numerical calculations we consider the 2D model.

Prior to the numerical calculations, we present illustrations to support the involved analytical findings. We adopted the material parameters of nickel: the saturation magnetization is $M_s = 4.8\times10^5$ A/m, the exchange constant is $A_{\rm ex} = 4.6\times10^{-12}$ A/m, the damping constant is $\alpha = 0.01$, the mass density is $\rho = 8908$ kg/m^3, the heat capacity is $C = 502$ J/(kg K), the thermal conductivity is $k_{ph} = 91$ W/(m K), Young's modulus is $E = 200$ GPa, Poisson's ratio is $\sigma = 0.31$, and the linear thermal expansion coefficient is $\kappa = 1.3\times10^{-5}$ K^{-1}. For an exponential temperature profile we set the decay length as $\beta = 5\times10^6$ m^{-1}, $T_0 = 0$, and $Q_1/C = 50$ K. The result for the exponential temperature profile $T(\mathbf{R}_1) = \frac{q}{C}\exp(-\beta|\mathbf{R}_1|) + T_0$ is shown in Fig. 1. As we can see, the temperature profile is isotropic and symmetric in the xy plane. The temperature is maximal in the area heated by the laser and decays exponentially with increasing distance from the laser spot. The symmetry properties of the displacement tensors u_x and u_y for an exponential temperature profile are quite intriguing (see Fig. 2). We clearly observe that the u_x component possesses a mirror symmetry with respect to reflection $y \to -y$ and is antisymmetric with respect to the reflection $x \to -x$. Concerning the component u_y, the situation is the opposite: it is symmetric with respect to the reflection $x \to -x$ and antisymmetric with respect to $y \to -y$. In the case of the linear temperature gradient (see Fig. 3) the symmetry properties of the displacement vector are preserved, but the maximum is slightly shifted to the edges of the sample $|\mathbf{u}(\mathbf{R})| = 2R_{\max}/3$. The components of the deformation tensor ϵ_{xx}, ϵ_{yy}, and ϵ_{xy} for the extended heat source are shown in Figs. 4, 5, and 6, and those for the linear temperature profile are shown in Fig. 7. The diagonal components ϵ_{xx} and ϵ_{yy} are larger but localized, while the

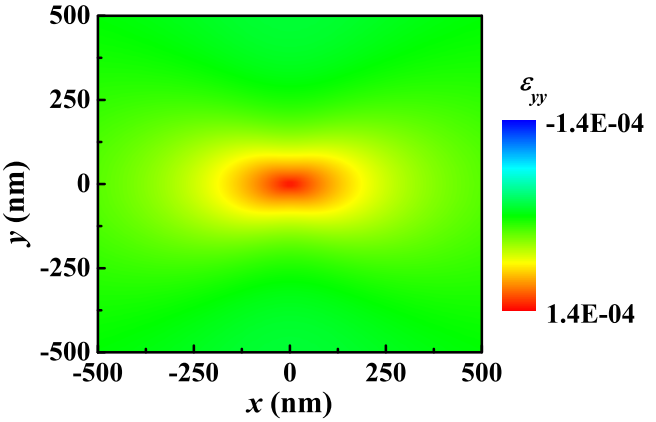

FIG. 5. The deformation tensor in the 3D bulk system ϵ_{yy}, induced by an exponential temperature profile (extended heat source) $T(\mathbf{R_1}) = \frac{Q_1}{C}\exp(-\beta|\mathbf{R_1}|)$. The density of the heat released by the laser $Q_1/C = 50$ K, and the heat capacity of the nickel $C = 502$ J/(kg K).

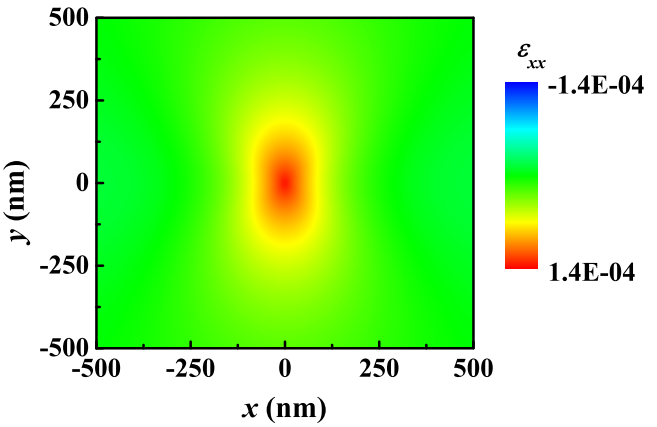

FIG. 4. The deformation tensor in the 3D bulk system ϵ_{xx} induced by an exponential temperature profile (extended heat source) $T(\mathbf{R_1}) = \frac{Q_1}{C}\exp(-\beta|\mathbf{R_1}|)$. The density of the heat released by the laser $Q_1/C = 50$ K, and the heat capacity of the nickel $C = 502$ J/(kg K).

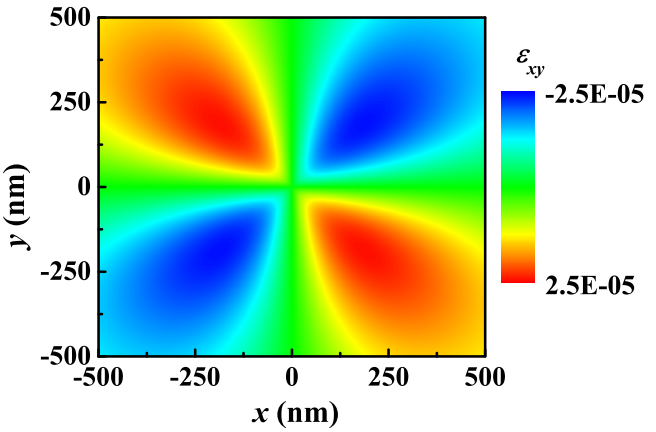

FIG. 6. The deformation tensor in the 3D bulk system ϵ_{xy}, induced by an exponential temperature profile (extended heat source) $T(\mathbf{R_1}) = \frac{Q_1}{C}\exp(-\beta|\mathbf{R_1}|)$. The density of the heat released by the laser $Q_1/C = 50$ K, and the heat capacity of the nickel $C = 502$ J/(kg K).

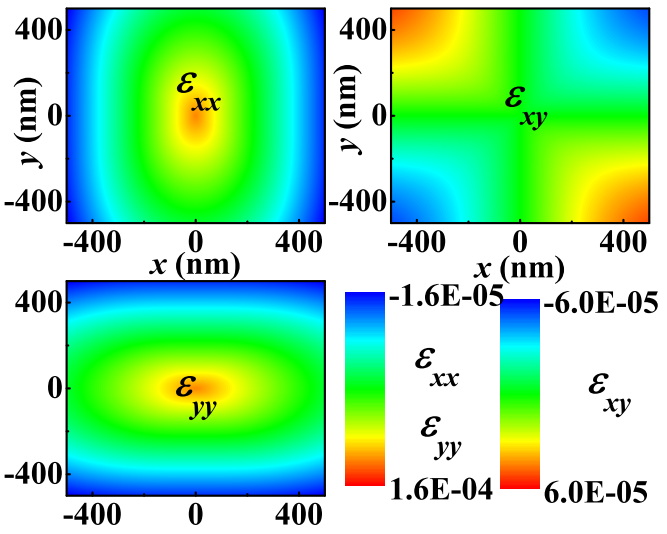

FIG. 7. The deformation tensors in the 3D bulk system ϵ_{xx}, ϵ_{yy}, and ϵ_{xy}, induced by a linear temperature profile. The temperature in the center is equal to $T(0) = 50$ K, and that at the edges is $T(R_{\max}) = 0$.

nondiagonal component of the deformation tensor ϵ_{xy} decays slower with distance and is finite in the whole sample.

The reduction in the magnonic gap can be illustrated as follows: The magnonic frequency $\omega(q,\mathbf{R},\boldsymbol{\varepsilon}_{\xi\zeta}(\mathbf{R}))$ increases with q. Suppose the following equation holds: $\omega(q_1,\mathbf{R_1},\boldsymbol{\varepsilon}_{\xi\zeta}(\mathbf{R_1})) = \omega(q_2,\mathbf{R_2},\boldsymbol{\varepsilon}_{\xi\zeta}(\mathbf{R_2}))$ for $q_1 > q_2$. This means that in the vicinity of $\mathbf{R_1}$ the magnetoelastic coupling degrades the magnonic frequency and around $\mathbf{R_2}$ increases it. Thus, by the constraint $\omega(q,\mathbf{R},\boldsymbol{\varepsilon}_{\xi\zeta}(\mathbf{R})) = \text{const}$ we can explore the function $q(\mathbf{R})$ or its inverse function. Using the exponential temperature profile and the analytically derived deformation tensor $\boldsymbol{\varepsilon}_{\xi\zeta}(\mathbf{R})$, the dispersion relation is calculated based on Eq. (20) with $H_0 = 3\times10^5$ A/m. For a fixed frequency $f = \omega/(2\pi) = 15$ GHz, the profile of $q(x,y)$ is shown in Fig. 8(a). Similar to the temperature profile $T(x,y)$ the symmetry features of the magnon profile manifest isotropy in the xy plane. In the center $(x = 0, y = 0)$, q reaches a minimum. The value of q increases gradually with distance from the center, reaching a maximum and beginning to decrease near to the boundary. Since $\omega(q,\mathbf{R},\boldsymbol{\varepsilon}_{\xi\zeta}(\mathbf{R}))$ is fixed, an increase in the wave vector is compensated by a negative contribution of the deformation tensor $\boldsymbol{\varepsilon}_{\xi\zeta}(\mathbf{R})$ in the magnon dispersion relation. Therefore, the maximum of q for a given fixed frequency $\omega(q,\mathbf{R},\boldsymbol{\varepsilon}_{\xi\zeta}(\mathbf{R}))$ corresponds to a minimum in the magnonic gap. We further calculate the elastic shift of the dispersion relations for different values of the coordinate x and a fixed value of the $y = 0$ coordinate, as shown in Fig. 8(b). As we see, the magnetoelastic effect either can increase the magnonic gap [Fig. 8(b)] or may decrease depending on the geometry of the sample and on the parameters. We note that the value of the gap is a local quantity that depends on $\mathbf{R}$.

V. THERMOELASTIC DISPERSION RELATIONS IN THIN MAGNETIC FILMS

Having explored the 3D case of a bulk system, we derive the thermoelastic dispersion relations for a thin 2D magnetic film.

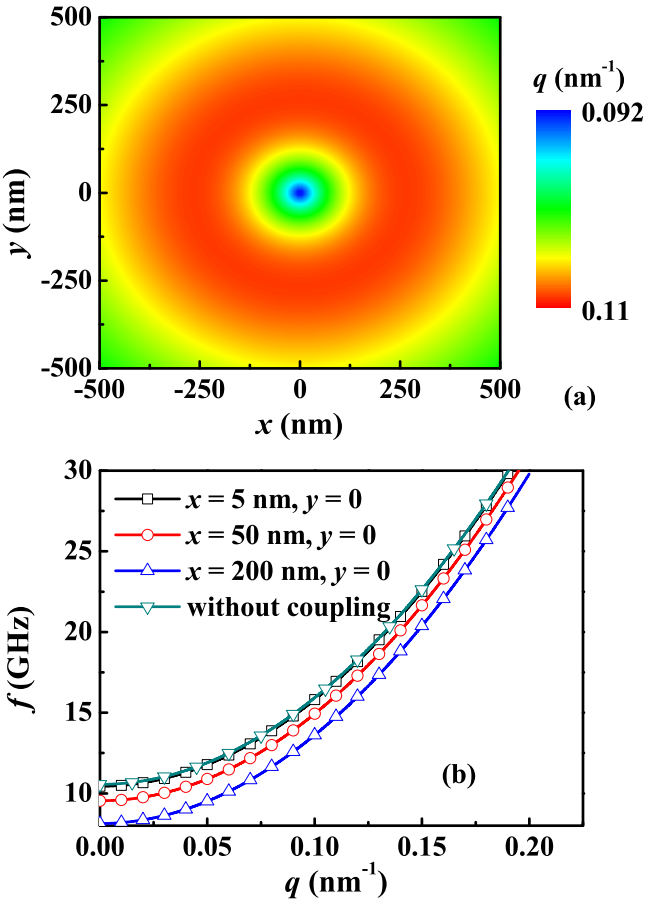

FIG. 8. (a) The profile of the wave vector $q(x,y)$ in the 3D bulk system $f = \omega(q,\mathbf{R})/(2\pi)$. The spatial distribution of magnons with the same fixed frequency $f = \omega(q,\mathbf{R})/(2\pi) = 15$ GHz but different wave vectors q is plotted. (b) For selectively chosen areas, $x = 5,50,200$ nm, $z = 0$, and $y = 0$, the dispersion relation of magnons is calculated using the analytical result (20). Values of the parameters are $A_{\text{ex}} = 4.6\times10^{-12}$ J/m, $\gamma = 1.76\times10^{11}$ (T s)$^{-1}$, $M_s = 4.8\times10^5$ A/m, $H_0 = 3\times105$ A/m, $B_1 = B_2 = 7.85\times10^8$ J/m^3.

The solution of the elasticity equation for the displacement vector reads

$$\mathbf{u}(\mathbf{R}) = \chi \int [T(\mathbf{R}_1) - T_0] \frac{\mathbf{R} - \mathbf{R}_1}{(R - R_1)^2} d^2\mathbf{R}_1,$$
$$\chi = \frac{\kappa(1+\sigma)}{6\pi(1-\sigma)}. \tag{30}$$

Similar to the 3D case, for a 2D thin film we consider pointlike and extended heat sources.

A. Pointlike heat source

In particular for the pointlike heat source $T(\mathbf{R}_1) - T_0 = \frac{Q}{C}\delta(\mathbf{R}_1)$ we infer

$$\mathbf{u}(\mathbf{R}) = \chi \frac{Q\mathbf{R}}{C R^2}, \tag{31}$$

while for the deformation tensor we obtain

$$\varepsilon_{\xi\zeta} = \frac{\chi Q}{C}\left(\frac{\delta_{\xi\zeta}}{R^2} - \frac{2x_\xi x_\zeta}{R^4}\right). \tag{32}$$

We note that the plane deformation tensor $\varepsilon_{\xi\zeta}$ has three independent components: $\varepsilon_{xx},\varepsilon_{yy},\varepsilon_{xy}=\varepsilon_{yx}$.

We already see the difference from the bulk system. Instead of $1/|\mathbf{R}^2|$ for the bulk system [Eq. (13)], for the 2D thin magnetic film the displacement vector decays slower $1/|\mathbf{R}|$. The same applies to the deformation tensor (32).

The magnetoacoustic energy density of the thin film has the form

$$U_{\text{mel}}(R)=\frac{B_1}{M_s^2}\left(M_x^2\varepsilon_{xx}+M_y^2\varepsilon_{yy}\right)+\frac{2B_2}{M_s^2}M_xM_y\varepsilon_{xy}, \quad (33)$$

and the effective magnetoacoustic field is

$$H_{xeff}=-\frac{2B_1}{M_s^2}\varepsilon_{xx}M_x-\frac{2B_2}{M_s^2}\varepsilon_{xy}M_y,$$
$$H_{yeff}=-\frac{2B_2}{M_s^2}\varepsilon_{yx}M_x-\frac{2B_1}{M_s^2}\varepsilon_{xx}M_x. \quad (34)$$

Utilizing Eqs. (8), (33), and (34) and assuming that the ground-state magnetization is aligned parallel to the z axis, we derive the following dispersion relation of the coupled magnetoelastic magnonic modes in the thin films:

$$\omega(q,R)=\frac{1}{\hbar}\sqrt{\left(Aq^2+g_D^{(1)}\right)\left(Aq^2+g_D^{(2)}\right)-g_D^{(3)}},$$
$$g_D^{(1)}=\hbar\gamma\left(H_0+\frac{2B_1}{M_s^2}\varepsilon_{xx}\right),$$
$$g_D^{(2)}=\hbar\gamma\left(H_0+\frac{2B_1}{M_s^2}\varepsilon_{yy}\right),$$
$$g_D^{(3)}=\left(\hbar\gamma\frac{2B_2}{M_s^2}\varepsilon_{xy}\right)^2. \quad (35)$$

As we see from Eq. (35), the dispersion relation is defined by the external field H_0 and the deformation tensor $\varepsilon_{\xi\zeta}$.

B. Extended heat source

In order to explore the effect of the extended heat source we solve the heat equation (11):

$$\frac{\partial^2T(x,y)}{\partial x^2}+\frac{\partial^2T(x,y)}{\partial y^2}=-aI(x,y),\quad a=\frac{\rho C}{k_{ph}}. \quad (36)$$

We adopt the source term $I=I_0e^{-\alpha(x+y)}$, with a positive characteristic decay constant $\alpha>0$ and the following boundary conditions: $x>0,y>0$. Then, the stationary solution of Eq. (36) reads

$$T(x,y)=-\frac{aI_0}{2\alpha^2}e^{-\alpha(x+y)}+T_0,$$
$$\alpha>0,\quad x>0,\quad y>0. \quad (37)$$

Taking into account Eq. (37) for the displacement vector and the deformation tensor, we deduce the following solutions:

$$u_x(x,y)=-\chi\frac{aI_0}{2\alpha^2}\int_0^\infty\int_0^\infty e^{-\alpha(x_1+y_1)}\frac{(x-x_1)dx_1dy_1}{(R-R_1)^2},$$
$$u_y(x,y)=-\chi\frac{aI_0}{2\alpha^2}\int_0^\infty\int_0^\infty e^{-\alpha(x_1+y_1)}\frac{(y-y_1)dx_1dy_1}{(R-R_1)^2} \quad (38)$$

and

$$\varepsilon_{xx}=-\varepsilon_{yy}$$
$$=\chi\frac{aI_0}{2\alpha^2}\int_0^\infty\int_0^\infty e^{-\alpha(x_1+y_1)}\frac{(x-x_1)^2-(y-y_1)^2}{(R-R_1)^4}dx_1dy_1,$$
$$\varepsilon_{xy}=\varepsilon_{yx}$$
$$=\chi\frac{aI_0}{\alpha^2}\int_0^\infty\int_0^\infty e^{-\alpha(x_1+y_1)}\frac{(x-x_1)(y-y_1)}{(R-R_1)^4}dx_1dy_1,$$
$$(R-R_1)^2=(x-x_1)^2+(y-y_1)^2. \quad (39)$$

The obtained result is quite involved in general and can be made transparent by numerical simulations. In the isotropic case, the problem simplifies, and we obtain an analytical solution in a closed form.

C. Extended isotropic heat source

We assume that the source term is isotropic $I=I_0e^{-\alpha R}$ and the temperature is a function of only R. Utilizing polar coordinates and performing the integration over the angle, we obtain from Eq. (36)

$$\frac{1}{R}\frac{\partial}{\partial R}\left(R\frac{\partial T(R)}{\partial R}\right)=-aI(R). \quad (40)$$

We adopt the boundary condition $T(R\to\infty)=T_0$ and find the stationary solution of the heat equation in the following form:

$$T(R)-T_0=-\frac{I_0}{\alpha^2}[\Gamma(0,\alpha R)+e^{-\alpha R}]. \quad (41)$$

Here $\Gamma(\alpha,z)=\int_z^\infty t^{\alpha-1}e^{-t}dt$ is the incomplete gamma function.

Taking into account the temperature profile (41), for the displacement vector and the deformation tensor we deduce the following solutions:

$$u_x=-\chi\frac{I_0}{\alpha^2}\int_0^\infty\int_0^{2\pi}[\Gamma(0,\alpha R')+e^{-\alpha R'}]$$
$$\times\frac{R\cos\theta-R'\cos\theta'}{R^2+R'^2-2RR'\cos(\theta-\theta')}R'dR'd\theta', \quad (42)$$
$$u_y=-\chi\frac{I_0}{\alpha^2}\int_0^\infty\int_0^{2\pi}[\Gamma(0,\alpha R')+e^{-\alpha R'}]$$
$$\times\frac{R\sin\theta-R'\sin\theta'}{R^2+R'^2-2RR'\cos(\theta-\theta')}R'dR'd\theta'. \quad (43)$$

After performing the integration for the displacement vector and the deformation tensor, we arrive at the expressions

$$u_x=-\chi\frac{3\pi I_0}{2\alpha^4}\frac{x}{R^2}, \quad (44)$$
$$u_y=-\chi\frac{3\pi I_0}{2\alpha^4}\frac{y}{R^2} \quad (45)$$

and

$$\varepsilon_{xx}=-\varepsilon_{yy}=\chi\frac{3\pi I_0}{2\alpha^4}\frac{x^2-y^2}{R^4}, \quad (46)$$
$$\varepsilon_{xy}=\varepsilon_{yx}=\chi\frac{3\pi I_0}{\alpha^4}\frac{xy}{R^4}. \quad (47)$$

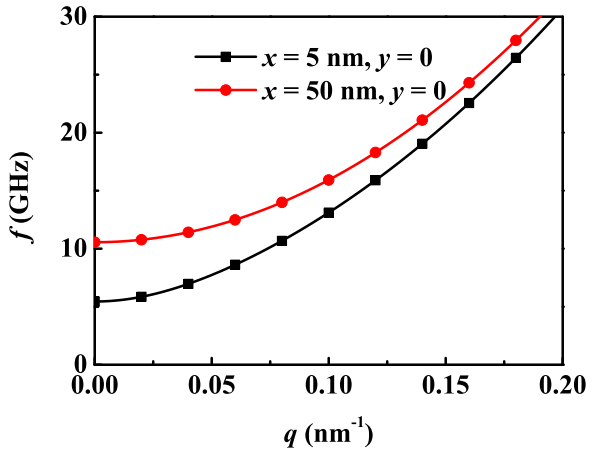

FIG. 9. For the 2D thin magnetic film and $x = 5{,}50$ nm and $y = 0$, the dispersion relation calculated using Eq. (35) and the following values of the parameters: $A_{ex} = 4.6\times10^{-12}$ J/m, $\gamma = 1.76\times10^{11}$ (T s)$^{-1}$, $M_s = 4.8\times10^5$ A/m, $H_0 = 3\times105$ A/m, $B_1 = B_2 = 7.85\times10^8$ J/m^3, $-I_0/\alpha = 0.01$ K, $\alpha = 5\times10^6$ m^{-1}, $\kappa = 1.3\times10^{-5}$ K^{-1}, and $\sigma = 0.31$.

Here $R^2 = x^2 + y^2$ is the in-plane radius vector. In order to obtain the dispersion relations in a closed form, we use Eqs. (44)–(46) in Eq. (35). Plots of the displacement vector, the deformation tensor, and the dispersion relation in the case of a 2D extended heat source are presented in Fig. 9. As we can see, the magnon dispersion relation is local and is different in the different areas of the film.

D. Linear temperature profile in thin magnetic films

We consider again a linear temperature profile of the following form: $T(R) = -(T' - T_0)R/R_{max} + T'$, where $T' > T_0$ and the temperature at the edges is equal to $T(0) = T'$,

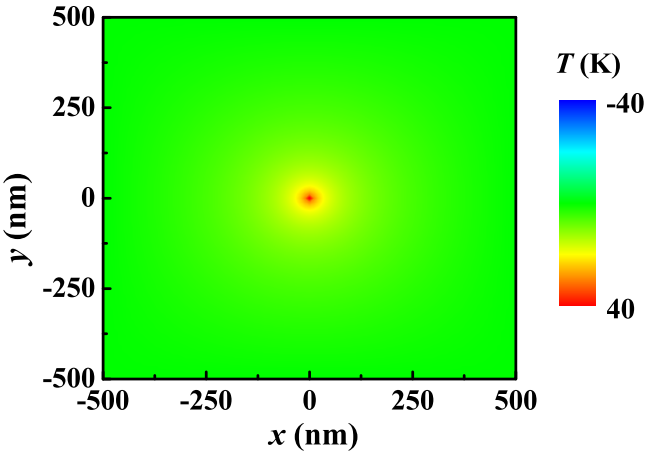

FIG. 10. For the 2D thin magnetic film, the steady-state spatial temperature profile formed in the system due to laser heating. The result is obtained via a numerical solution of the heat equation. The maximum temperature in the area heated by laser pulses is $T_0 = 40$ K in the vicinity of the point $x = 0$ and $y = 0$ and decays gradually to zero with the distance.

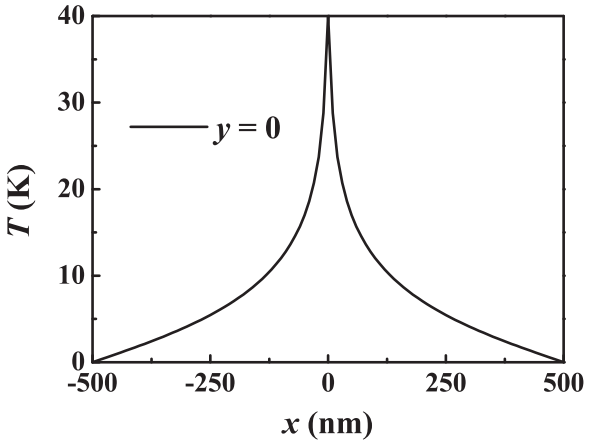

FIG. 11. For the 2D thin magnetic film, the projective plot of the steady-state spatial temperature profile formed in the system due to laser heating following the numerical solution of the heat equation.

$T(R_{max}) = T_0$. The displacement vector behaves as

$$u_x = -\chi(T_0 - T')\frac{\pi R_{max}^2}{6}\frac{x}{R^2}, \tag{48}$$

$$u_y = -\chi(T_0 - T')\frac{\pi R_{max}^2}{6}\frac{y}{R^2}, \tag{49}$$

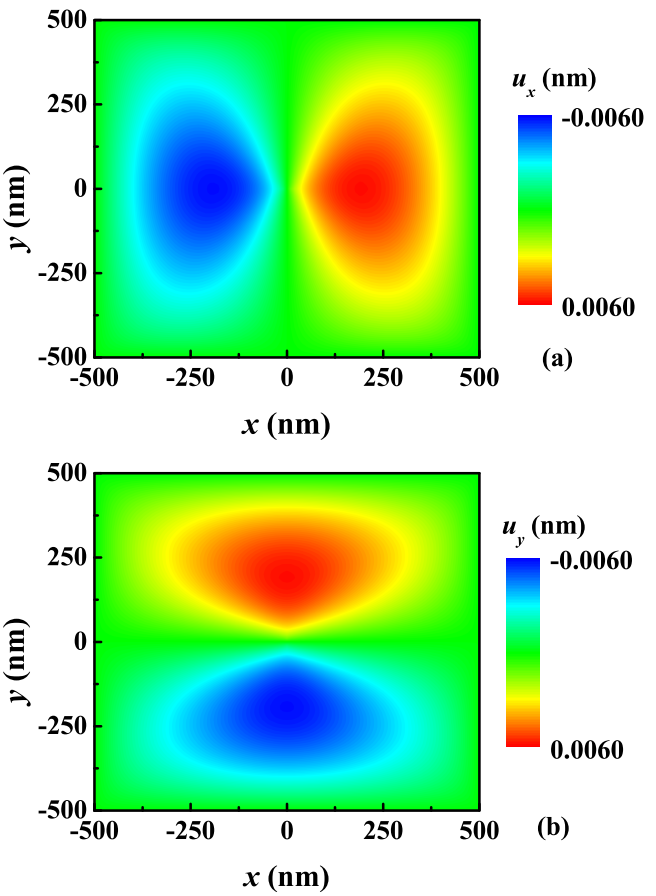

FIG. 12. For the 2D thin magnetic film, the steady-state spatial profile of the displacement vectors (a) u_x and (b) u_y.

and the deformation tensor reads

$$\varepsilon_{xx} = -\varepsilon_{yy} = \chi(T_0 - T')\frac{\pi R_{\max}^2}{6}\frac{x^2 - y^2}{R^4}, \quad (50)$$

$$\varepsilon_{xy} = \varepsilon_{yx} = \chi(T_0 - T')\frac{\pi R_{\max}^2}{6}\frac{xy}{R^4}. \quad (51)$$

As is evident, a linear temperature profile in thin magnetic films leads to asymptotic decay: $1/R$ for the displacement vector and $1/R^2$ for the deformation tensor.

VI. NUMERICAL RESULTS

The numerical simulations are performed for a two-dimensional nickel film. The external field with $H_z = 4.5\times10^5$ A/m is applied along the x axis, leading to a uniform ground state. A two-dimensional ferromagnetic thin film with a length of 1000 nm is aligned along the x axis and has a width of 1000 nm in the y direction. We also assume that the source term that enters in the heat equation and describes the effect of the laser heating is a local function, $I(\mathbf{R},t) = \delta(\mathbf{R} - \mathbf{R}_0)$, corresponding to the case when the intensity of the laser field is spatially localized. This approximation is similar to the local heat source model discussed analytically in the previous sections. We assume the heating laser spot is around ($x = 0$ nm, $y = 0$ nm). The thermal effect of the laser heating is described by the heat equation (11) using the fixed boundary conditions

$$T(x = 500\text{ nm}) = 0,$$
$$T(x = -500\text{ nm}) = 0,$$
$$T(y = 500\text{ nm}) = 0, \quad T(y = -500\text{ nm}) = 0. \quad (52)$$

The value of the temperature T_0 formed in the area of the heating laser depends on the laser intensity I. For the boundary conditions (52) implemented numerically in the heat equation (11) we obtain the stable spatial temperature profile. As inferred from Fig. 10, the temperature profile $T(x,y)$ shows an exponential decay with the distance from $T_0(x = 0, y = 0)$. This numerical result for the temperature profile is in good agreement with the assumptions used for the analytical solution. The exponential character of the decay of the temperature profile is more evident from Fig. 11.

The heat diffusion induces a thermal gradient ∇T and an elastic deformation in the system. Using the equation of elasticity (7), we find numerically the temperature profile $T(x,y)$ and calculate the components of the displacement vector for the following fixed boundary conditions:

$$\mathbf{u}(x = 500\text{ nm}) = (0,0,0),$$
$$\mathbf{u}(x = -500\text{ nm}) = (0,0,0),$$
$$\mathbf{u}(y = -500\text{ nm}) = (0,0,0),$$
$$\mathbf{u}(y = 500\text{ nm}) = (0,0,0). \quad (53)$$

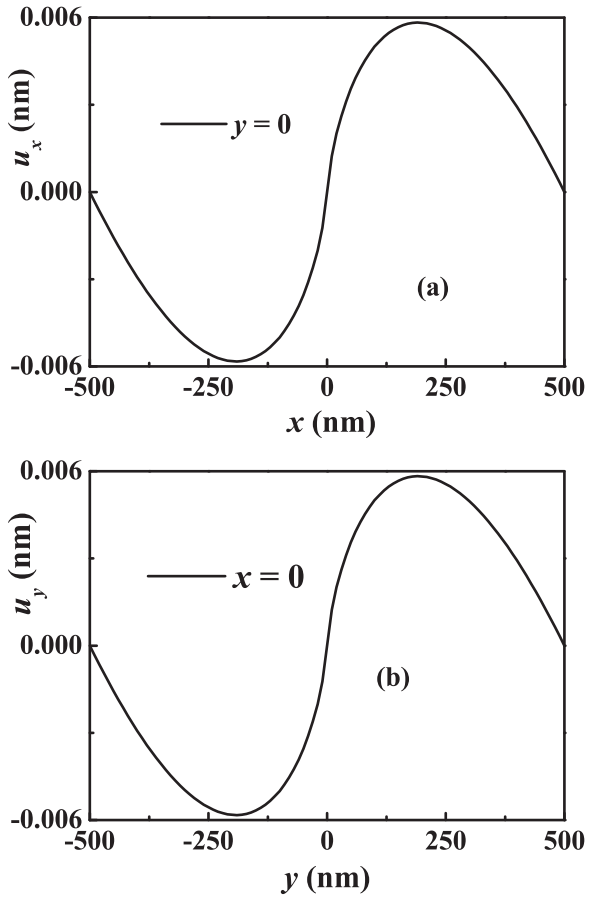

FIG. 13. For the 2D thin magnetic film, the steady-state spatial profile of the displacement vectors (a) u_x at $y = 0$ and (b) u_y at $x = 0$.

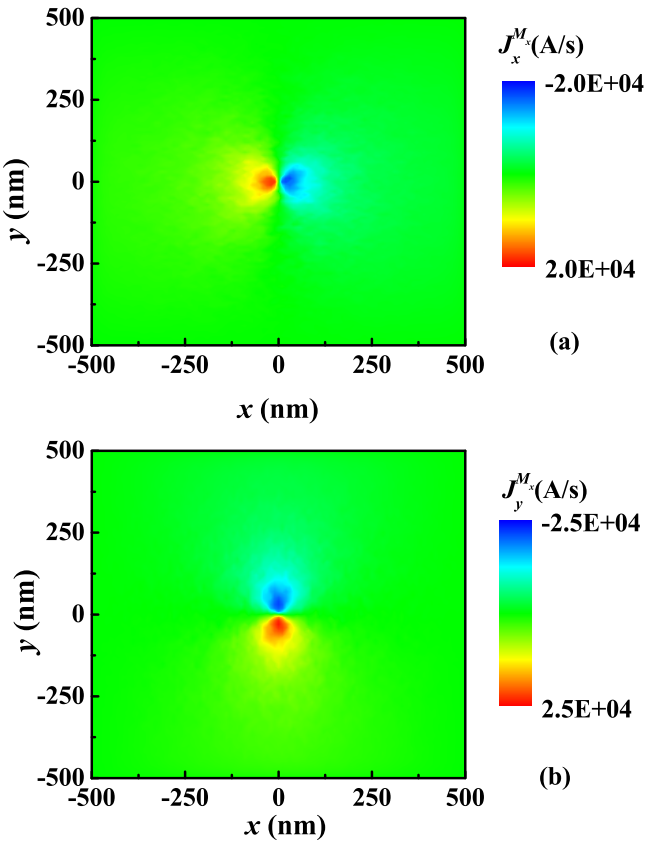

FIG. 14. For the 2D thin magnetic film, the steady-state spatial profile of the components of the magnonic spin current tensors (a) $J_x^{M_x}$ and (b) $J_y^{M_x}$ with an elastic term when $T_0 = 80$ K.

The steady-state components of the elastic displacement vectors u_x and u_y are shown in Figs. 12 and 13. We recognize a certain similarity with the previously obtained analytical results. Namely, we clearly see that the u_x component exhibits mirror symmetry with respect to the reflection $y \to -y$ and is antisymmetric with respect to the reflection $x \to -x$. Concerning the component u_y, the situation is reversed: symmetry is given for $x \to -x$, and antisymmetry is given for $y \to -y$. The components of the deformation tensor ϵ_{xx}, ϵ_{yy}, and ϵ_{xy} are shown in Figs. 4, 5, and 6. The diagonal components ϵ_{xx} and ϵ_{yy} are larger but localized, while the nondiagonal component of the deformation tensor ϵ_{xy} decays slower and remains finite in the whole sample.

We implement the numerically deduced temperature profile $T(x,y)$ and the elastic displacement profile $\mathbf{u}(x,y)$ in the stochastic Landau-Lifshitz-Gilbert equation (8). The existence of the thermal gradient formed in the system due to the laser heating may lead to the emergence of magnonic spin current and a longitudinal spin Seebeck effect. However, on top of this standard effect, the thermal heating leads to a thermal activation of the deformation tensor. Due to the magnetoelastic interaction the thermally activated deformation tensor contributes to the magnetization dynamics and modifies the net magnonic current. For $T_0 = 80$ K, the components of the magnonic spin current tensor $J_x^{M_x} = \frac{2\gamma A_{ex}}{\mu_0 M_s^2}(M_y \partial_x M_z - M_z \partial_x M_y)$ and $J_y^{M_x} = \frac{2\gamma A_{ex}}{\mu_0 M_s^2}(M_y \partial_y M_z - M_z \partial_y M_y)$ are plotted in Fig. 14.

Figure 15 shows that the magnon current emerges in the area heated by the laser pulses and propagates according to the formed thermal bias (which has been established swiftly on the magnon timescale). The $J_x^{M_x}$ and $J_y^{M_x}$ components of the spin current tensor are negative for $x > 0$ and $y > 0$, respectively, becoming positive in the rest of the sample. We observe a similar abrupt switching of the displacement vectors u_x and u_y in Fig. 12(b). To highlight the role of the elastic term in the magnonic spin current we plot the magnonic current in the presence and absence of the magnetoelastic contribution for the same thermal gradient. Figure 15 shows the profile of the magnonic spin current, in particular the tensor components $J_x^{M_x}$ and $J_y^{M_x}$. They have qualitatively the same behavior in the presence and in the absence of the magnetoelastic coupling. However, as shown in Fig. 16, the value of $J_y^{M_x}$ obviously becomes larger with the elastic term, while the change in $J_x^{M_x}$ due to the elastic term is marginal. We conclude that elasticity leads to the enhancement of the magnonic spin Seebeck current in certain directions. Also, the bias temperature is important. Raising T_0 and hence $\mathbf{u}$, the increase in the magnonic spin current J^{M_x} and the elastic enchantment of $J_y^{M_x}$ are evident, as shown in Fig. 17.

To understand the selective enhancement of the magnonic spin current induced by the magnetoelastic coupling we inspect the x component of the magnetoelastic effective field

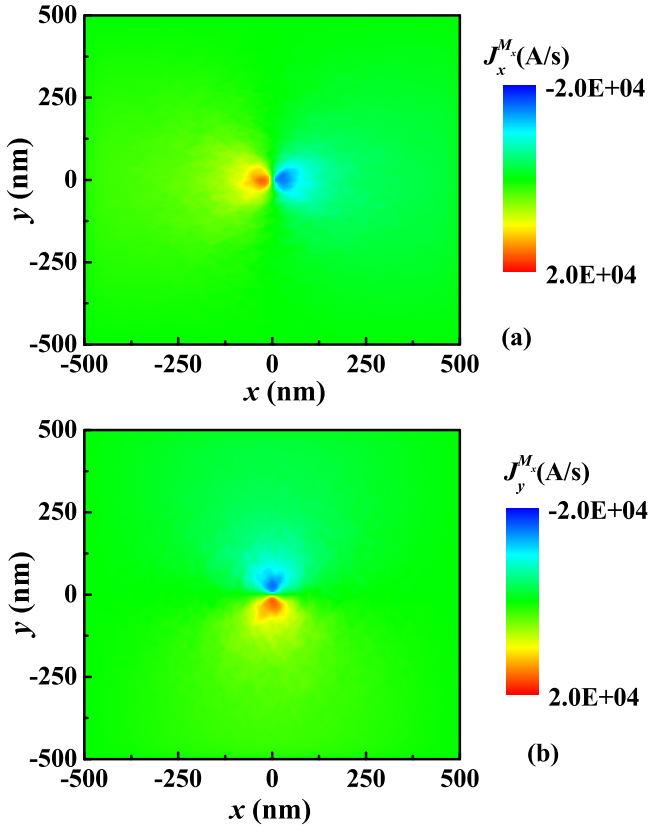

FIG. 15. For the 2D thin magnetic film, the steady-state spatial profile of the components of the magnonic spin current tensors in the absence of a magnetoelastic effect (a) $J_x^{M_x}$ and (b) $J_y^{M_x}$ when $T_0 = 80$ K.

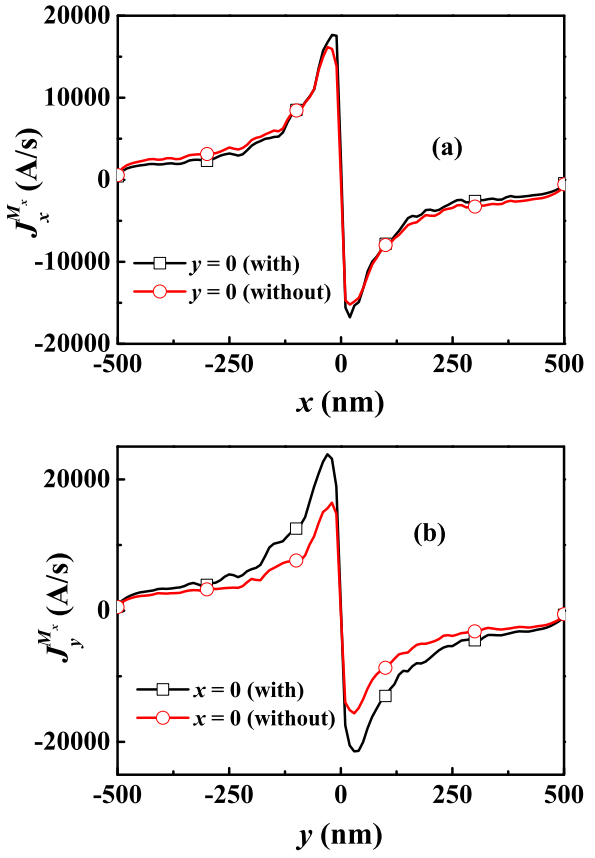

FIG. 16. For the 2D thin magnetic film, the steady-state spatial profile of the components of magnonic spin current tensor (a) $J_x^{M_x}$ at $y = 0$ and (b) $J_y^{M_x}$ at $x = 0$ with and without the magnetoelastic term.

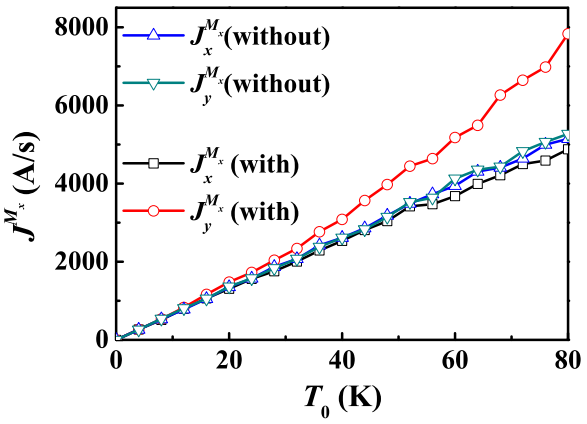

FIG. 17. For the 2D thin magnetic film, the averaged $J_x^{M_x}$ in $((-500)\text{ nm} < x < 0, y = 0)$ and $J_y^{M_x}$ in $(x = 0, (-500)\text{ nm} < y < 0)$ with and without the magnetoelastic term.

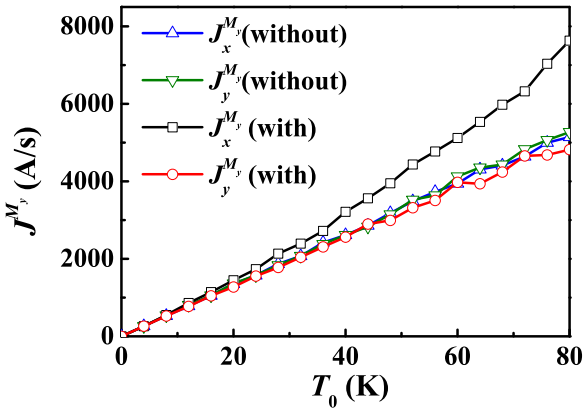

FIG. 19. For the 2D thin magnetic film, the averaged $J_x^{M_y}$ in $((-500)\text{ nm} < x < 0, y = 0)$ and $J_y^{M_y}$ in $(x = 0, (-500)\text{ nm} < y < 0)$ with and without the magnetoelastic term.

$H^{\text{eff}}_{ME-x} = -[\delta U_{\text{mel}}(\mathbf{R})/\delta \mathbf{M}(\mathbf{R})]_x$ in Fig. 18(a), which shows that the effective magnetoelastic field is directed opposite to the external field. Therefore, it reduces the gap in the magnon spectrum. By changing the equilibrium magnetization along $+y$, the distribution of the effective magnetoelastic field is changed [Fig. 18(b)], and the corresponding magnonic spin current, i.e., $J_x^{M_y}$, is selectively enhanced. This feature is further proved by Fig. 19. The maximal temperature in the center of the laser intensity is equal to $T_0 = 80$ K. For the experimental observation of the thermoelastic effect, we suggest exploiting the magnetization-sensitive thermoelastic effect and detecting the spin Seebeck effect for the different directions of the equilibrium magnetization.

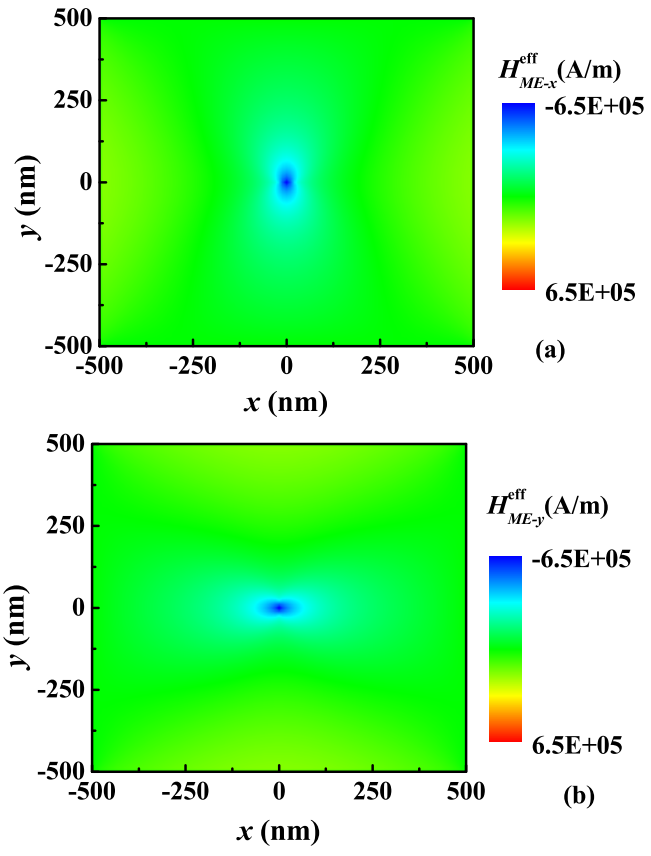

FIG. 18. For the 2D thin magnetic film, (a) the profile of the numerically obtained x component of the magnetoelastic effective field H^{eff}_{ME-x} with the equilibrium magnetization in the $+x$ direction and (b) the profile of the y component of the magnetoelastic effective field H^{eff}_{ME-y}, calculated numerically with the equilibrium magnetization in the $+y$ direction.

For a typical spin Seebeck experiment, the spin current is measured by means of the inverse spin Hall effect using an attached platinum detecting bar. The total net current $\mathbf{I} = \mathbf{I}_{sp} + \mathbf{I}_{fl}$ consists of two contributions: the spin pumping current $\mathbf{I}_{sp}$ flowing from the magnetic insulator towards the detecting bar and a backward spin current $\mathbf{I}_{fl} = -M_s \mathbf{m} \times \mathbf{h}$ injected from the detecting bar into the magnetic insulator [42]. Here $\mathbf{h}$ is the random magnetic field related to the platinum detecting bar. An interesting question is whether thermoelasticity is important for the backward spin current. To

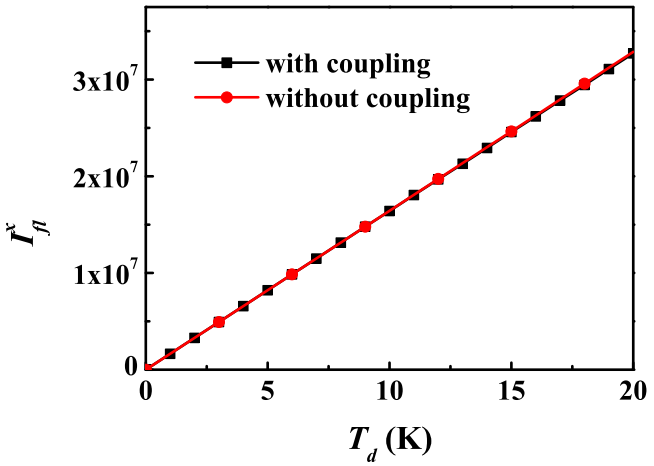

FIG. 20. For the 2D thin magnetic film, the x component of the backward spin current $\mathbf{I}^x_{fl}$ in the presence and absence of the thermoelastic effect. The temperature T_d of the detecting bar is uniform, while the temperature of the magnet is inhomogeneous. The equilibrium magnetization is along $+x$.

answer this question, we calculate the backward spin current $\mathbf{I}_{fl}$ in the presence and absence of the thermoelastic effect. The result of the numerical calculations is shown in Fig. 20. As we can see, thermoelasticity has no influence on the backward spin current.

VII. CONCLUSIONS

We studied the spin Seebeck effect in bulk samples and thin ferromagnetic films and explored the influence of the thermoelastic steady-state deformation on the magnonic spin current. For a particular temperature profile in the system, we obtained analytical expressions for the thermoelastic deformation tensor. We derived analytical results for both the 3D bulk system and 2D thin magnetic film. We observed that the displacement vector and the deformation tensor in bulk systems decay asymptotically as $u \sim 1/R^2$ and $\varepsilon \sim 1/R^3$, respectively. The decay in thin magnetic films is slower, with $u \sim 1/R$, and $\varepsilon \sim 1/R^2$. We found that due to the magnetoelastic coupling, the thermoelastic deformation tensor has a significant impact on the magnetization dynamics. We derived analytical expressions for the dispersion relations for thermoelastic magnons, highlighting a principal difference between the thermoelastic and magnetoelastic effects. Magnetoelastic effects always enhance the magnetoelastic gap in the magnonic spectrum. Thermoelastic steady-state deformation may lead either to an enchantment or to a reduction in the gap of the magnonic spectrum. A reduction in the gap increases the number of magnons contributing to the spin Seebeck effect, offering a thermoelastic control of the spin Seebeck effect.

ACKNOWLEDGMENTS

This work is supported by the DFG through the SFB 762 and SFB-TRR 227, as well as by the National Natural Science Foundation of China (Grant No. 11704415).

[1] A. I. Akhiezer, V. G. Beryakhtar, and S. V. Peletminsky, Zh. Eksp. Teor. Fiz. **35**, 228 (1958) [Sov. Phys. JETP **8**, 157 (1959)].
[2] C. Kittel, Phys. Rev. **110**, 836 (1958).
[3] A. S. Borovik-Romanov and K. G. Rudashevskii, Zh. Eksp. Teor. Fiz. **47**, 2095 (1964) [Sov. Phys. JETP **20**, 1407 (1965)].
[4] A. Tasaki and S. Iida, J. Phys. Soc. Jpn. **18**, 1148 (1963).
[5] E. A. Turov and V. G. Shavrov, Fiz. Tverd. Tela **7**, 217 (1965) [Sov. Phys. Solid State **7**, 166 (1965)].
[6] E. A. Turov and V. G. Shavrov, Sov. Phys. Usp. **26**, 593 (1983).
[7] D. Sander, Rep. Prog. Phys. **62**, 809 (1999).
[8] L. Dreher, M. Weiler, M. Pernpeintner, H. Huebl, R. Gross, M. S. Brandt, and S. T. B. Goennenwein, Phys. Rev. B **86**, 134415 (2012).
[9] J. Janusonis, C. L. Chang, P. H. M. van Loosdrecht, and R. I. Tobey, Appl. Phys. Lett. **106**, 181601 (2015); J. Janusonis, C.-L. Chang, T. Jansma, A. Gatilova, V. S. Vlasov, A. M. Lomonosov, V. V. Temnov, and R. I. Tobey, Phys. Rev. B **94**, 024415 (2016); J. Janusonis, T. Jansma, C.-L. Chang, Q. Liu, A. Gatilova, A. M. Lomonosov, V. Shalagatskyi, T. Pezeril, V. V. Temnov, and R. I. Tobey, Sci. Rep. **6**, 29143 (2016).
[10] A. V. Scherbakov, A. S. Salasyuk, A. V. Akimov, X. Liu, M. Bombeck, C. Brüggemann, D. R. Yakovlev, V. F. Sapega, J. K. Furdyna, and M. Bayer, Phys. Rev. Lett. **105**, 117204 (2010).
[11] J.-W. Kim, M. Vomir, and J.-Y. Bigot, Phys. Rev. Lett. **109**, 166601 (2012).
[12] L. Thevenard, J. Y. Duquesne, E. Peronne, H. J. von Bardeleben, H. Jaffres, S. Ruttala, J.-M. George, A. Lemaître, and C. Gourdon, Phys. Rev. B **87**, 144402 (2013).
[13] V. Iurchuk, D. Schick, J. Bran, D. Colson, A. Forget, D. Halley, A. Koc, M. Reinhardt, C. Kwamen, N. A. Morley, M. Bargheer, M. Viret, R. Gumeniuk, G. Schmerber, B. Doudin, and B. Kundys, Phys. Rev. Lett. **117**, 107403 (2016).
[14] O. Kovalenko, T. Pezeril, and V. V. Temnov, Phys. Rev. Lett. **110**, 266602 (2013).
[15] T. L. Linnik, A. V. Scherbakov, D. R. Yakovlev, X. Liu, J. K. Furdyna, and M. Bayer, Phys. Rev. B **84**, 214432 (2011).
[16] C. L. Jia, N. Zhang, A. Sukhov, and J. Berakdar, New J. Phys. **18**, 023002 (2016).
[17] X.-G. Wang, L. Chotorlishvili, and J. Berakdar, Front. Mater. **4**, 19 (2017).
[18] V. Kupradze, T. G. Gegelia, M. O. Basheleishvili, and T. V. Burchuladze, *Three-Dimensional Problems of the Mathematical Theory of Elasticity and Thermoelasticity* (North-Holland, Amsterdam, 1979).
[19] L. D. Landau and E. M. Lifshitz, *Theory of Elasticity*, 2nd ed. (Pergamon Press, Oxford, UK, 1970), Vol. 7.
[20] P. Yan, G. E. W. Bauer, and H. Zhang, Phys. Rev. B **95**, 024417 (2017).
[21] J. Barker and G. E. W. Bauer, Phys. Rev. Lett. **117**, 217201 (2016).
[22] G. Lefkidis and S. A. Reyes, Phys. Rev. B **94**, 144433 (2016).
[23] V. Basso, E. Ferraro, and M. Piazzi, Phys. Rev. B **94**, 144422 (2016).
[24] K. I. Uchida, H. Adachi, T. Kikkawa *et al.*, Proc. IEEE **104**, 1946 (2016).
[25] E. J. Guo, J. Cramer, A. Kehlberger, C. A. Ferguson, D. A. MacLaren, G. Jakob, and M. Klaui, Phys. Rev. X **6**, 031012 (2016)
[26] M. Schreier, F. Kramer, H. Huebl *et al.*, Phys. Rev. B **93**, 224430 (2016).
[27] V. Basso, E. Ferraro, A. Magni, A. Sola, M. Kuepferling, and M. Pasquale, Phys. Rev. B **93**, 184421 (2016).
[28] U. Ritzmann, D. Hinzke, A. Kehlberger, E. J. Guo, M. Klaui, and U. Nowak, Phys. Rev. B **92**, 174411 (2015).
[29] Z. Qiu, D. Hou, T. Kikkawa *et al.*, Appl. Phys. Express **8**, 083001 (2015).
[30] W. Jiang, P. Upadhyaya, Y. Fan, J. Zhao, M. Wang, L.-T. Chang, M. Lang, K. L. Wong, M. Lewis, Y.-T. Lin, J. Tang, S. Cherepov, X. Zhou, Y. Tserkovnyak, R. N. Schwartz, and K. L. Wang, Phys. Rev. Lett. **110**, 177202 (2013).
[31] S. R. Etesami, L. Chotorlishvili, A. Sukhov, and J. Berakdar, Phys. Rev. B **90**, 014410 (2014).
[32] L. Chotorlishvili, S. R. Etesami, J. Berakdar, R. Khomeriki, and J. Ren, Phys. Rev. B **92**, 134424 (2015).

[33] L. Chotorlishvili, Z. Toklikishvili, V. K. Dugaev, J. Barnaś, S. Trimper, and J. Berakdar, Phys. Rev. B **88**, 144429 (2013); A. Sukhov, L. Chotorlishvili, A. Ernst, X. Zubizarreta, S. Ostanin, I. Mertig, E. K. U. Gross, and J. Berakdar, Sci. Rep. **6**, 24411 (2016).

[34] X.-G. Wang, L. Chotorlishvili, G.-H. Guo, A. Sukhov, V. Dugaev, J. Barnaś, and J. Berakdar, Phys. Rev. B **94**, 104410 (2016).

[35] K.-i. Uchida, T. An, Y. Kajiwara, M. Toda, and E. Saitoh, Appl. Phys. Lett. **99**, 192102 (2011).

[36] M. Weiler, H. Huebl, F. S. Goerg, F. D. Czeschka, R. Gross, and S. T. B. Goennenwein, Phys. Rev. Lett. **108**, 176601 (2012).

[37] T. Crimmins, A. Maznev, and K. Nelson, Appl. Phys. Lett. **74**, 1344 (1999); R. I. Tobey, M. E. Siemens, M. M. Murnane, H. C. Kapteyn, D. H. Torchinsky, and K. A. Nelson, *ibid.* **89**, 091108 (2006).

[38] S. R. Boona and J. P. Heremans, Phys. Rev. B **90**, 064421 (2014); M. Agrawal, V. I. Vasyuchka, A. A. Serga, A. D. Karenowska, G. A. Melkov, and B. Hillebrands, Phys. Rev. Lett. **111**, 107204 (2013); N. Roschewsky, M. Schreier, A. Kamra, F. Schade, K. Ganzhorn, S. Meyer, H. Huebl, S. Geprgs, R. Gross, and S. T. B. Goennenwein, Appl. Phys. Lett. **104**, 202410 (2014); Y. Yahagi, B. Harteneck, S. Cabrini, and H. Schmidt, Phys. Rev. B **90**, 140405(R) (2014).

[39] S. R. Etesami, L. Chotorlishvili, and J. Berakdar, Appl. Phys. Lett. **107**, 132402 (2015).

[40] K. Uchida, S. Takahashi, K. Harii, J. Ieda, W. Koshibae, K. Ando, S. Maekawa, and E. Saitoh, Nature (London) **455**, 778 (2008).

[41] H. Adachi, J.-i. Ohe, S. Takahashi, and S. Maekawa, Phys. Rev. B **83**, 094410 (2011).

[42] J. Xiao, G. E. W. Bauer, K.-c. Uchida, E. Saitoh, and S. Maekawa, Phys. Rev. B **81**, 214418 (2010).